



Tuning Ag-modified NaTaO₃ to achieve high CO selectivity for the photocatalytic conversion of CO₂ using H₂O as the electron donor

Xuanwen Xu^a, Hiroyuki Asakura^{a,b}, Saburo Hosokawa^{a,c}, Tsunehiro Tanaka^{a,b},
Kentarō Teramura^{a,b,*}

^a Department of Molecular Engineering, Graduate School of Engineering, Kyoto University, Kyotodaigaku Katsura, Nishikyo-ku, Kyoto 615–8510, Japan

^b Elements Strategy Initiative for Catalysts & Batteries (ESICB), Kyoto University, 1–30 Goryo-Ohara, Nishikyo-ku, Kyoto 615–8245, Japan

^c Faculty of Materials Science and Engineering, Kyoto Institute of Technology, Matsugasaki, Sakyo-ku, Kyoto 606–8585, Japan

ARTICLE INFO

Keywords:

NaTaO₃

Ag nanoparticles

CO₂ photoreduction

CO

Selectivity and stability

ABSTRACT

Ag-loaded NaTaO₃ was used for the photocatalytic conversion of CO₂ using H₂O as the electron donor, and the effect of the nanoparticle size, Ag loading, and crystal structure on the photocatalytic activity and CO selectivity were investigated. The sizes of the Ag nanoparticles could be tuned by controlling the photodeposition time, and relatively larger Ag nanoparticles were found to show higher CO selectivity. During the photocatalytic reaction, the initially polycrystalline Ag nanoparticles became single crystalline owing to the dissolution and redeposition of Ag, and the change in morphology reduced the CO selectivity. To solve this problem, Ag–Cr dual cocatalysts having a core–shell structure were developed. Subsequently, the locations and sizes of the Ag nanoparticles on the surfaces of NaTaO₃ were maintained during the reaction because of the protection by the chromium shell, thus providing stable and selective CO production via the photocatalytic conversion of CO₂ by H₂O.

1. Introduction

Since the first industrial revolution, humans have been dependent on fossil fuels. Although renewable energy sources, such as wind [1] and hydro [2] power are now in use, fossil fuels are still the main energy source. However, CO₂, a potent greenhouse gas, is emitted during the combustion of fossil fuels [3], and this has resulted in global warming [4]. Therefore, the exploitation of solar energy as a replacement for fossil fuels using photovoltaic cells [5], photocatalytic conversion of biomass [6], H₂O splitting [7], and CO₂ conversion [8], has drawn attention. In particular, the photocatalytic conversion of CO₂ by H₂O is a promising pathway for the capture and reuse of CO₂, thus storing solar energy and contributing to the fight against global warming. The products from the photocatalytic conversion of CO₂ with H₂O as the electron donor are H₂ and molecules derived from CO₂. In this process (see Eq. (1)), syngas [9], which consists of H₂ and CO, is always produced. In contrast, the production of other organic species, including CHOOH, CH₃OH, and CH₄, requires high overpotentials. As a result, they were rarely produced in aqueous solutions. The successful photocatalytic conversion of CO₂ by H₂O should satisfy the balance (close to

1.0) between the consumed photogenerated electrons and holes, as shown in Eq. (2). Note that C_x (x > 1) compounds such as C₂H₄ are not calculated into Eq. (2) because they are very difficult to be produced in the photocatalytic conversion of CO₂ in aqueous solutions. The production of a stoichiometric amount of O₂ in the reaction is an important indicator that the electrons used in the reaction originate from H₂O rather than sacrificial reagents, such as carbon impurities, which are typically present. Note that the Eq. (2) is reasonable only when there are no liquid products being produced in the reactions. Otherwise, liquid products may establish the other balance close to 1.0 with possible H₂O₂ [10].

$$\text{Selectivity} = R_{\text{CO}} / (R_{\text{CO}} + R_{\text{H}_2}) \times 100\% \quad (1)$$

$$e^-/h^+ = (R_{\text{CO}} + R_{\text{H}_2})/2R_{\text{O}_2} \quad (2)$$

CO is an important precursor in the production of a range of industrial reagents such as aldehydes, polycarbonates, and polyurethanes. Therefore, the production of CO with high selectivity in the photocatalytic conversion of CO₂ using H₂O as an electron donor is attractive. Ag-modified MLa₄Ti₄O₁₅ (M = Ca, Sr, and Ba) [11], which was first

* Corresponding author at: Department of Molecular Engineering, Graduate School of Engineering, Kyoto University, Kyotodaigaku Katsura, Nishikyo-ku, Kyoto 615–8510, Japan.

E-mail address: teramura@moleng.kyoto-u.ac.jp (K. Teramura).

<https://doi.org/10.1016/j.apcatb.2022.121885>

Received 1 June 2022; Received in revised form 18 August 2022; Accepted 20 August 2022

Available online 13 September 2022

0926-3373/© 2022 Published by Elsevier B.V.

reported by Kudo et al., was the first photocatalyst to produce CO in quantities exceeding those of H₂ for this reaction. Recently, Ag nanoparticles have been used as cocatalysts and have been found to show high selectivity toward the evolution of CO over other photocatalysts for CO₂ reduction, such as CaTiO₃ [12], K₂Ti₆O₁₃ [13], SrNb₂O₆ [14], and ZnGa₂O₄ [15]. Although many types of photocatalysts modified with Ag nanoparticles can satisfy Eq. (2), few produce CO with high selectivity; examples of these photocatalysts include Ta₂O₅ (18%) [16], NaTaO₃ (4%) [17], ZnTa₂O₆ (43.4%) [18], Ga₂O₃ (40%) [19], and Na₂Ti₆O₁₃ (60%) [20]. Further, basic metal oxides have been used to modify Ag-loaded photocatalysts for the photocatalytic conversion of CO₂ by H₂O, for example, NaTaO₃:Sr(Ca) [17], SrO/Ta₂O₅ [16], Al/SrTiO₃ [21], ZnO/ZnTa₂O₆ [22], and ZnO/Ga₂O₃ [23]. In previous studies, we compared the effects of various metal cocatalysts, including Ag, Pt, Au, Ni, Cu [18], and Pd [24] on ZnTa₂O₆ for the photocatalytic conversion of CO₂ by H₂O, and the results showed that only Ag nanoparticles resulted in high selectivity toward CO. In addition, we observed that the conversion of CO₂ and CO selectivity also depended on the amount and size of Ag nanoparticles, which can be easily controlled by adjusting the loading method (impregnation, photodeposition, or chemical reduction) used [12,15]. Hori et al. [25] found that the morphology of the Ag electrode had a significant effect on CO evolution in the electrochemical reduction of CO₂. The partial current density for CO production over the Ag (110) facet was remarkably higher than those of the (111) and (100) facets, and we also observed this in our previous work, in which we found that Ag electrodes pretreated with O₃ had higher activity and CO selectivity at the same applied voltages than those that had not received pretreatment [26]. Further, the importance of the structure of the metal cocatalyst used for the selective reduction of CO₂ was also confirmed in a study of Au electrodes, which are rich in grain boundaries [27,28].

The use of dual cocatalysts, such as Ag/M (M: Cr [29], Co [30], Mn [31], and Fe [32]), has also been reported to promote the production of CO in the photocatalytic conversion of CO₂ using H₂O as an electron donor dramatically. However, although they are considered to follow the same mechanism, the Ag/Co and Ag/Fe dual cocatalysts did not perform in the same way regarding the stability of CO production. In particular, the Ag/Co dual cocatalyst showed poor stability.

Therefore, we have found that the activity, CO selectivity, and stability of catalysts for the photocatalytic conversion of CO₂ using H₂O as an electron donor depend on many factors, such as the surface modification and morphology of the photocatalyst, size and microstructure of the metal cocatalyst, and presence of dual cocatalysts. In this work, we tuned the size and number of Ag nanoparticles loaded on NaTaO₃ by optimizing the photodeposition time and carried out surface modification with chromium(III) species and investigated the effects of these modifications on the selectivity and stability of CO evolution during the photocatalytic conversion of CO₂ by H₂O.

2. Experimental section

2.1. Synthesis of photocatalysts

NaTaO₃ (NTO) was synthesized using a solid-state reaction. Stoichiometric amounts of Ta₂O₅ and Na₂CO₃ were ground together well and calcined at 1423 K for 20 h in an aluminum crucible. Ag nanoparticles were loaded onto the photocatalysts via photodeposition (precursor: AgNO₃, H₂O: 1 L, Ar: 30 mL min⁻¹, Jacket: quartz, photo-irradiation: 400 W high-pressure Hg lamp). The photodeposition time and amount of Ag precursor were controlled to investigate their effects on photocatalyst performance. In addition, dual cocatalysts (Ag/M, M = Cr, Cu, Mo, Fe, or Mn) were obtained by the co-photodeposition of AgNO₃ and Na₂CrO₄, Cu(NO₃)₂, Na₂MoO₄, Fe(NO₃)₃, and KMnO₄, respectively.

2.2. Photocatalyst characterization

The morphologies of the photocatalysts were observed using field-emission scanning electron microscopy (FE-SEM, SU-8220, Hitachi High-Technologies) at an accelerating voltage of 3.0–5.0 kV and emission current of 10 μ A. The microstructures of the Ag nanoparticles were characterized by transmission electron microscopy (TEM, JEM-2100 F, JEOL). The X-ray diffraction (XRD) patterns of the synthesized NaTaO₃ samples were obtained using a Rigaku Ultima IV powder diffractometer (Cu-K α radiation, 40 kV, 40 mA). The absorption spectra of the Ag nanoparticles were recorded using a JASCO V-670 spectrometer. To determine the chemical states of the loaded Ag nanoparticles, X-ray photoelectron spectroscopy (XPS) measurements were conducted using an ESCA 3400 instrument (Shimadzu Corp.). Leached ions in solution were examined using inductively coupled plasma–optical emission spectrometry (ICP-OES, iCAP7400, Thermo Fisher Scientific, Inc.).

2.3. Photocatalytic reaction procedure

The equipment used for the photocatalytic conversion of CO₂ by H₂O is depicted in Fig. S1. An inner irradiation reactor with a quartz jacket was connected to cooling water, and the temperature during the reactions was controlled between 298 and 303 K. A 400-W high-pressure mercury lamp (Sen Lights Corp.) was used as the light source. The products derived from H₂O and CO₂ were detected using gas chromatography (GC, GC-8A, Shimadzu Corp.) using a thermal conductivity detector (TCD) and flame ionization detector (FID), respectively.

3. Results and discussion

3.1. Morphology of NaTaO₃

The XRD pattern presented in Fig. 1 shows that the pure NaTaO₃ (NTO) phase was successfully obtained through the solid-state reaction method used in this work, even though trace unknown impurity peaks were observed. The (100) and (110) [33,34] facets were obtained after calcination, as confirmed by the SEM image of the synthesized NTO (Fig. 2), which shows that the particles were nearly cubic in shape

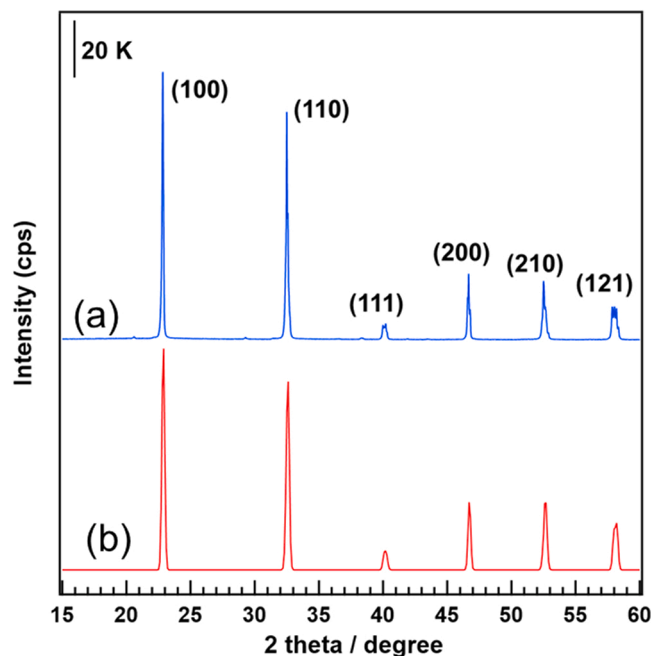


Fig. 1. XRD pattern of (a) synthesized NaTaO₃ and (b) the Inorganic Crystal Structure Database (ICSD) reference pattern (No. 88375).

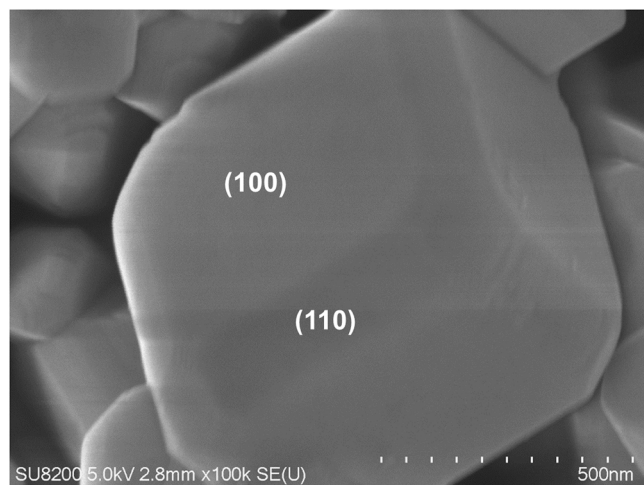


Fig. 2. SEM image of synthesized NaTaO₃.

enclosed by the (100) and (110) facets. As a typical perovskite material, perfect NaTaO₃ should have a cubic habit. The formation of the (110) facet indicates that sodium and oxygen defects were formed in the NTO during calcination. Undoubtedly, some sodium species evaporated during calcination because the Na₂CO₃ precursor has a low melting point. This means that the sodium component in the final product was not stoichiometric with the tantalum component. For comparison, Na-poor and Na-rich NTO samples were synthesized by tuning the ratio of Na⁺ to Ta⁵⁺ (0.9 and 1.1, respectively) in the precursors. Fig. S2(a) shows that larger (110) facets were formed in the Na-poor NTO sample compared with the NTO fabricated from a stoichiometric amount of Na⁺ and Ta⁵⁺ precursors. However, the formation of the (110) facet was almost completely inhibited when 10 mol% of excess sodium precursor was used to prepare Na-rich NTO (Fig. S2(b)). Based on the XRD patterns of the Na-poor and Na-rich NTO samples in Fig. S3, it is clear that the intensity of the diffraction arising from the (110) facet in the Na-rich NTO is much lower than that of the Na-poor NTO. Therefore, it is reasonable to conclude that the formation of the (110) facet in NTO is

caused by the loss of sodium species during calcination.

3.2. Photodeposition time for Ag nanoparticle loading

Fig. 3 shows SEM images of Ag nanoparticles on the surface of the NTO particles prepared by photodeposition for different periods. Large numbers of Ag nanoparticles were observed on the (100) facet when the photodeposition time was 0.5 h, as shown in Fig. 3(a). However, the number of Ag particles decreased significantly when the photodeposition time was increased to 1 h, as shown in Fig. 3(b), and the number of particles decreased further when the photodeposition time was increased to 3 and 5 h. In particular, there are very few Ag nanoparticles on the surface of NTO after 3 h of photodeposition (Fig. 3(c)), and they are absent after photodeposition for 5 h (Fig. 3(d)), possibly as a result of the presence of very small-sized Ag nanoparticles. Strangely, a small number of Ag nanoparticles were observed again when the photodeposition time was increased to 7 and 12 h, as shown in Fig. 3(e) and (f), indicating the growth of the nanoparticles after these times. The pH before photodeposition of Ag nanoparticles was about 4.8 because of the presence of AgNO₃. After 0.5 h of photodeposition, the pH increased to 3.9 probably caused by the reduction of Ag⁺ and leaving H⁺ and NO₃⁻ in the solution. when the photodeposition time was prolonged to 12 h, the pH increased to about 5.2. Next, we performed ICP-OES measurements of the sample solutions after photodeposition to determine the Ag loading. Based on the analysis of the remaining reaction solution, almost 100% of the precursor Ag had been loaded onto the surface of NTO after 0.5 h photodeposition (Fig. S4). Similarly, no Ag⁺ ions were found in solution after photodeposition for up to 12 h, indicating that the Ag nanoparticles initially photodeposited on the surface of NTO were not leached into the solution during longer photoirradiation periods.

Fig. 4 shows the UV-Vis diffuse reflectance spectra of the Ag/NTO photocatalysts prepared using different photodeposition times. Peaks originating from the surface plasmon resonance (SPR) were observed in the spectra of the Ag/NTO samples at 382 and 465 nm. Ag or Au nanoparticles with heterogeneous sizes in close distance to each other will exhibit obvious coupling of SPR, which results in the splitting of SPR peaks [35]. Therefore, these two peaks were probably caused by the coupling of the resonance of adjacent Ag particles having heterogeneous

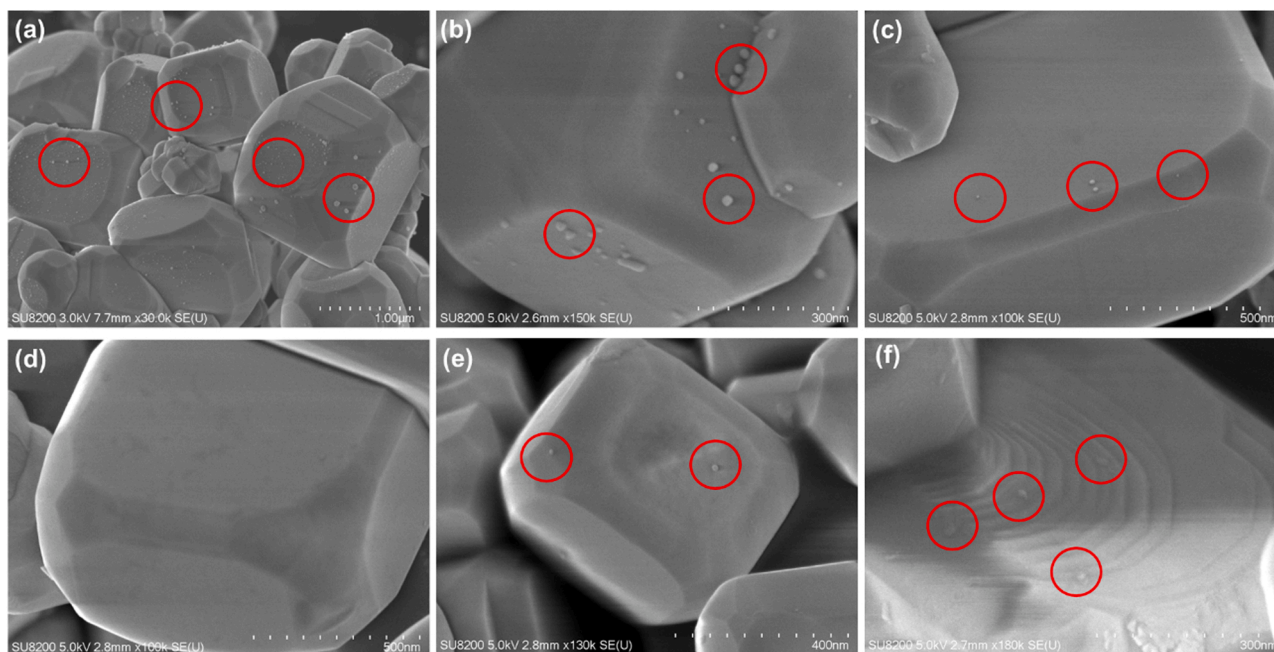


Fig. 3. SEM images of Ag/NTO prepared at photodeposition times of (a) 0.5, (b) 1, (c) 3, (d) 5, (e) 7, and (f) 12 h. Ag nanoparticles are highlighted with red circles. Ag loading: 0.29 wt%.

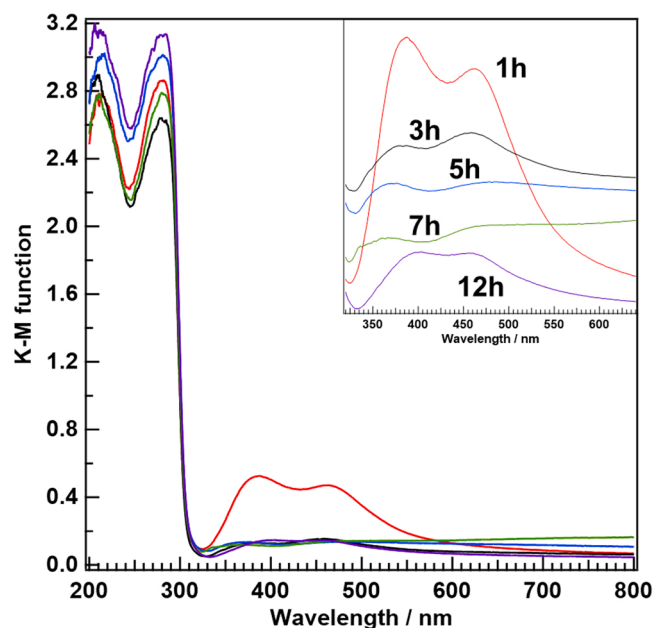


Fig. 4. UV-Vis diffuse reflectance spectra of Ag/NTO prepared using different photodeposition times. Ag loading: 0.29 wt%. Inset shows an enlarged image of the SPR peaks arising from the Ag nanoparticles. K-M = Kubelka-Munk function.

sizes in Fig. 4. However, the peak intensities of the Ag nanoparticles decreased with increase in the photodeposition time from 1 to 7 h but increased slightly when the photodeposition time was prolonged to 12 h, again indicating that the size of the Ag nanoparticles increased. Next, the chemical states of the Ag nanoparticles were characterized using XPS. The peaks at 368 and 352 eV in the 3d Ag XPS (368 eV) and Auger electron spectra (352 eV) did not change, as shown in Figs. S5(a) and S5(b), which indicates that the chemical state of the nanoparticles was not affected by the photodeposition time. The Auger parameters revealed that all nanoparticles comprised Ag^0 (720.0 eV), which is easily distinguished from Ag^+ (718.5 eV) and Ag^{2+} (718.9 eV).

Fig. 5 shows the activity and selectivity of the prepared photocatalysts toward CO evolution during the photocatalytic conversion of CO_2 by H_2O . The rate of formation of O_2 , which indicates the total photocatalyst activity (see Eq. (2)), increased gradually for the samples

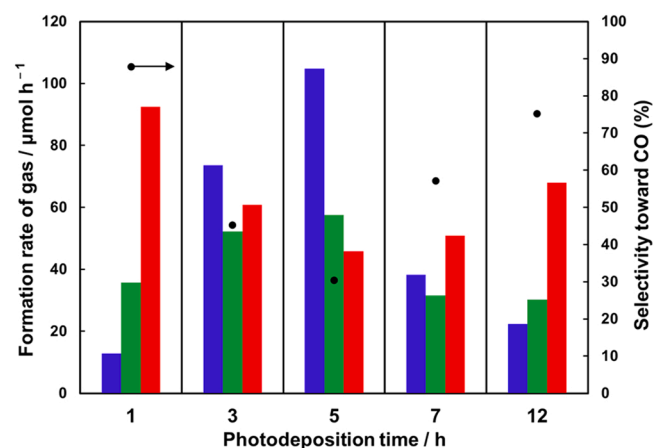


Fig. 5. Formation rates of H_2 (blue), O_2 (green), and CO (red) and CO selectivity (black dots) for the photocatalytic reaction over Ag/NTO prepared using different photodeposition times. Photocatalyst: 0.5 g; Ag loading: 0.29 wt%; photoirradiation time: 1 h; reaction solution: 1 L of aqueous 0.1 M NaHCO_3 ; CO_2 flow rate: 30 mL min^{-1} ; light source: 400-W high-pressure Hg lamp

photodeposited for 1–5 h ($36\text{--}57 \mu\text{mol h}^{-1}$) and then decreased in the samples photodeposited for periods up to 12 h ($30 \mu\text{mol h}^{-1}$). The same trend was observed in overall water splitting over bare NTO (Fig. S6); this trend arises because there is a trade-off relationship between Na^+ leaching from the surface of NTO and the growth of the (110) facet over time. We also observed an increase in the pH from 6.6 to 8.0 during the reaction, and there are two explanations for this: (1) protons could be strongly adsorbed on the surfaces of NTO or (2) protons could be exchanged for Na^+ on the surfaces. Both scenarios would cause an increase in the pH because OH^- would be left in the bulk solution. By comparing the XRD patterns (Fig. S7) before and after the photocatalytic reaction, it was found that the intensity of the diffraction corresponding to the (110) facet increased relative to that of the (100) facet after reaction, indicating that the (110) facets grew selectively. This can be confirmed by comparing the SEM images before and after the photocatalytic reaction (see Figs. S8(a) and S8(b)). As shown in these images, the smooth (100) facet became rough owing to the formation of the (110) facet. Based on Fig. S2, it is reasonable to conclude that the formation of the (110) facet during the water splitting reaction is caused by the leaching of Na^+ ions from the (100) facet to the solution. Therefore, we believe that the change in pH was caused by ion exchange between the Na^+ ions in the NTO framework and the protons in the solution, which resulted in a high concentration of OH^- near the NTO surfaces under photoirradiation. This was then confirmed by ICP measurement on concentration of Na^+ ($32.0 \mu\text{mol L}^{-1}$) in the solution after H_2O splitting over bare NTO. Therefore, we carried out Ag nanoparticle loading onto NTO under high pH (11.4) conditions (Fig. S9) and found that larger Ag nanoparticles were formed. Therefore, the observed decrease in the size of the Ag particles with increasing photodeposition time should not be caused by the rapid increase in pH arising from ion exchange. As discussed, with increase in photodeposition time, the number of active sites on NTO increased and subsequently decreased as a result of the trade-off between the formation of the (110) facet and leaching of Na^+ . The former enhances the separation of charge carriers between the (100) and (110) facets, whereas the latter inevitably creates more defects on the surfaces of NTO, which results in the increased recombination of photogenerated electrons and holes. Metal nanoparticles, such as Pt, have been reported to act as recombination centers for photogenerated electrons and holes when they exceed specific sizes [36,37]. This means that photogenerated holes, as well as electrons, could be capable of migrating to the Ag nanoparticles under photoirradiation. We believe that the reduction of Ag^+ and oxidation of Ag^0 reaches dynamic equilibrium during photoirradiation, and Ag^0 would be redeposited on the surfaces of NTO, thus resulting in changes to the number of active sites under photoirradiation, as well as changes to the size of the Ag nanoparticles.

Interestingly, the CO selectivity of Ag/NTO was significantly influenced by the photodeposition time. Specifically, the large Ag nanoparticles (1 h) produced CO as the main product with an activity of $92 \mu\text{mol h}^{-1}$, and the CO selectivity reached 88%. For the sample photodeposited for 5 h, the CO formation rate decreased to $46 \mu\text{mol h}^{-1}$, and the H_2 formation rate increased from 13 to $105 \mu\text{mol h}^{-1}$. Thus, the selectivity toward CO evolution shows a “V”-like trend, reaching 75% with a CO formation rate of $67 \mu\text{mol h}^{-1}$ for the sample photodeposited for 12 h. Therefore, the CO selectivity is dependent on the size of the Ag nanoparticles, as shown in Figs. 3 and 5. In addition, the chemical state of Ag^0 was maintained both before and after the reaction (Figs. S5 and S10).

3.3. Amount of Ag loaded on NTO

The photodeposition time and Ag loading also affect the size of the Ag nanoparticles. Fig. 6 shows SEM images of Ag/NTO particles prepared with different Ag loadings. The Ag nanoparticles produced using 0.02, 0.05, and 0.10 wt% of the Ag precursor were too small to be observed, as shown in Fig. 6(a–c), and the size of the Ag nanoparticles

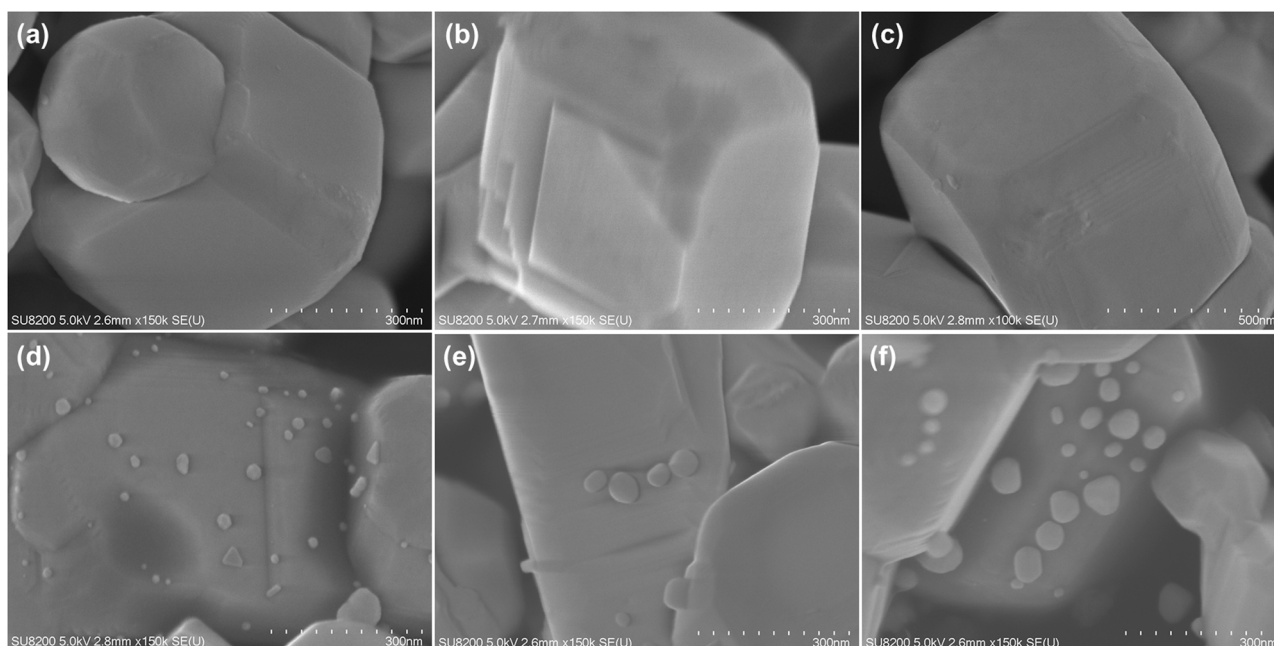


Fig. 6. SEM images of Ag/NTO catalysts prepared with different Ag loadings: (a) 0.02, (b) 0.05, (c) 0.1, (d) 0.6, (e) 1.0, and (f) 3.0 wt%. Photodeposition time: 1 h.

increased gradually with increase in Ag loading, as shown in Fig. 6(d–f). However, the density of the Ag nanoparticle dispersion did not change significantly. This indicates that the successful reduction of Ag^+ ions in the precursor solutions proceeded on the surfaces of the previously deposited small Ag nanoparticles, and these particles grew slowly. Crucially, if further growth had not occurred on the initially deposited seed particles, the density of Ag particles would have increased. Based on the Section 3.2 discussion, the Ag nanoparticles of 0.29 wt% Ag/NTO should be capable of scavenging the photogenerated electrons completely from the surface of NTO because the density of Ag nanoparticles did not increase with an increase in the loading amount. Next, we monitored the H_2 , O_2 , and CO formation rates for the photocatalytic reaction over Ag/NTO, as shown in Fig. 7. The CO selectivity varied significantly with respect to Ag loading from 0.02 to 3.0 wt%. In addition, the formation rate of H_2 was increased significantly with an increase of loading amount of Ag nanoparticles from 0.02 to 1.0 wt% during the reaction. Interestingly, the formation rate of H_2 formation rate was not almost changed over 5 h of reaction in the case of the 3.0 wt % Ag/NTO. This unstable performance is not a result of changes in the

surface properties of NTO during the photocatalytic reaction because bare NTO showed stable performance under the same conditions (Fig. S11). Further, the stability and selectivity in the CO evolution decreased gradually for all samples, regardless of the Ag loading.

Fig. 8 displays SEM images of Ag/NTO particles prepared with different Ag loadings after the photocatalytic reaction. For the sample prepared with a Ag loading of 0.6 wt%, the size of the Ag nanoparticles decreased from 30 nm before reaction to 20 nm after reaction. The size-reduction phenomenon was even more significant for the catalyst prepared with a Ag loading of 0.29 wt%, for which the Ag nanoparticles disappeared after the reaction. In contrast, for the sample prepared with a Ag loading of 0.60 wt%, the particles after the reaction (Fig. 8(b)) remained larger than those prepared with 0.29 wt% Ag before the reaction (15 nm) (Fig. 3(b)). This result reveals that the change in the CO formation rate was not caused by a decrease in the size of the Ag nanoparticles. Fig. 9 shows the TEM images of the Ag/NTO catalyst prepared with a Ag loading of 0.29 wt% before and after the reaction. The lattice fringes of the Ag nanoparticles before the reaction indicate a polycrystalline structure, showing growth in multiple directions, as well

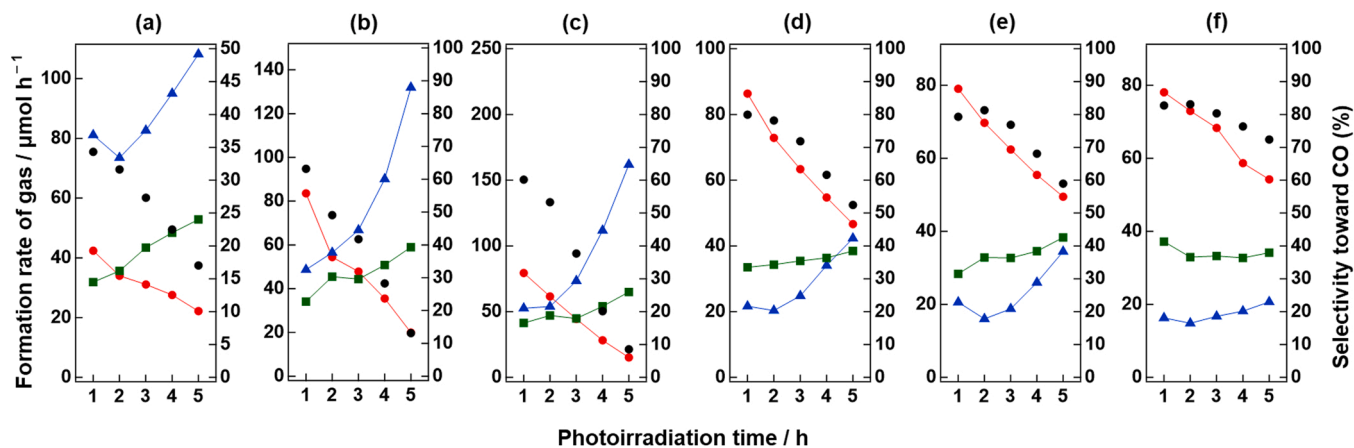


Fig. 7. Formation rates of H_2 (blue), O_2 (green), and CO (red) and CO selectivity (black dots) with respect to time during the photocatalytic reaction over Ag/NTO prepared with different Ag loadings: (a) 0.02, (b) 0.05, (c) 0.1, (d) 0.6, (e) 1.0, and (f) 3.0 wt%. Photocatalyst: 0.5 g; reaction solution: 1 L of aqueous 0.1 M NaHCO_3 ; CO_2 flow rate: 30 mL min^{-1} ; light source: 400-W high-pressure Hg lamp. Photodeposition time for Ag loading: 1 h.

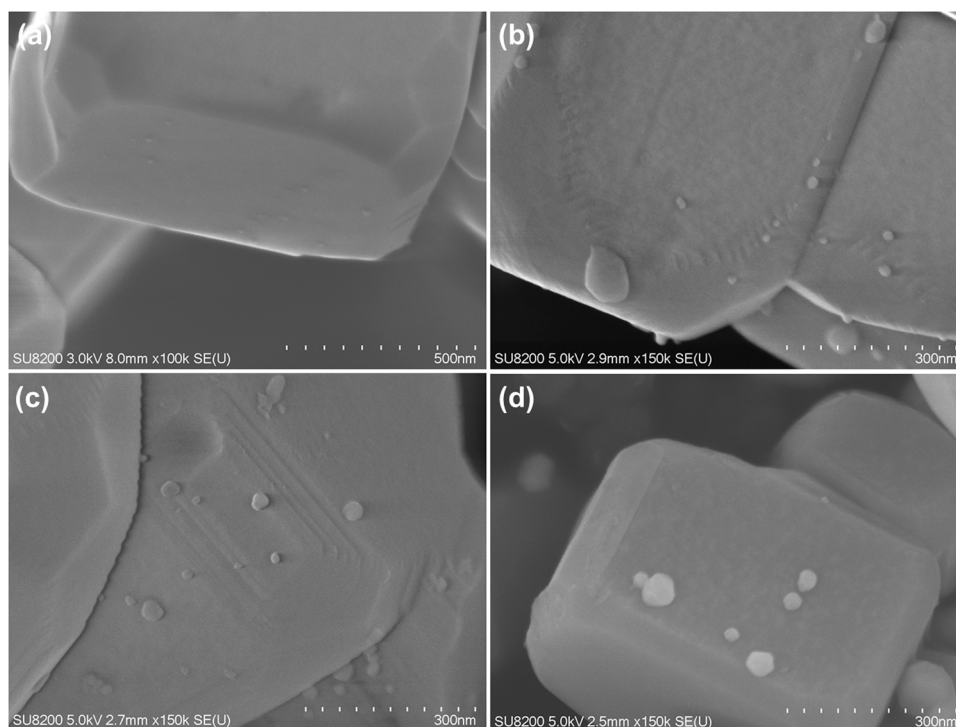


Fig. 8. SEM images of catalyst particles after the photocatalytic reaction. Ag/NTO was prepared with different Ag loadings: (a) 0.29, (b) 0.60, (c) 1.00, and (d) 3.00 wt%.

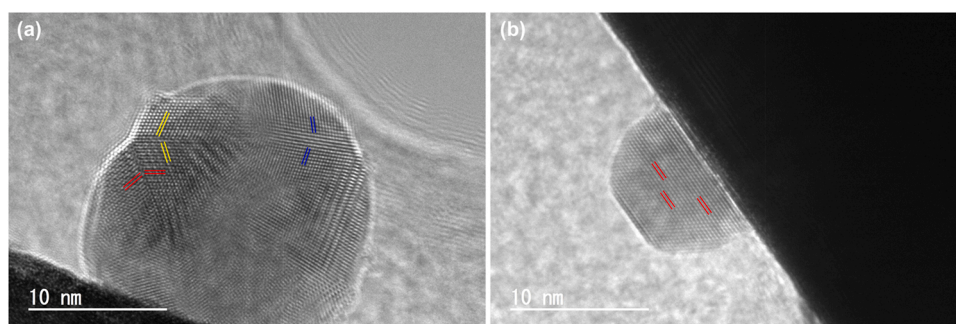


Fig. 9. TEM images of Ag/NTO (a) before and (b) after reaction. Amount of Ag: 0.29 wt%.

as the presence of a large number of grain boundaries (Fig. 9(a)). Interestingly, the Ag lattice planes became aligned after the reaction, indicating a transformation from a polycrystalline to single-crystalline structure, as shown in Fig. 9(b). Thus, during the photocatalytic reaction, the number of grain boundaries in the Ag nanoparticles is reduced. It has been widely reported that the presence of grain boundaries enhances the selectivity toward CO evolution in the electrochemical reduction of CO₂ [28,38,39], suggesting that the observed reduction in the number of grain boundaries in our catalyst would result in a reduction in the CO selectivity with time. Therefore, the poor stability in CO selectivity during the photocatalytic reaction is considered to be caused by the loss of grain boundaries in the Ag nanoparticles. Unfortunately, it was a little difficult to make statistics on the morphology changes of Ag nanoparticles because Ag nanoparticles were difficult to be observed on Ta-based supporting.

3.4. Effect of modification of the Ag nanoparticles: Ag@Cr core-shell

We previously reported that the addition of a shell of chromium hydroxide on Ag nanoparticles enhanced the CO selectivity of Ag-loaded Ga₂O₃ [24]. Therefore, we prepared a series of Ag/M (M = Cu, Mo, Fe,

Mn, or Cr) dual cocatalysts on NTO for the photocatalytic conversion of CO₂ by H₂O. The performance of the dual cocatalysts for this reaction are summarized in Table 1. Only the Ag@Cr cocatalyst prepared by the co-photodeposition of AgNO₃ and Na₂CrO₄ yielded a high CO selectivity (87.7% compared to 81.1% for the Ag/NTO catalyst). Next, XPS Ag 3d

Table 1

Formation rates of H₂, O₂, and CO and CO selectivity in the photocatalytic conversion of CO₂ using H₂O as an electron donor over Ag@M-loaded NTO.^a

Cocatalyst	Formation rate / $\mu\text{mol h}^{-1}$			Selec. To CO (%)
	H ₂	O ₂	CO	
Ag	12.9	35.7	92.4	87.7
Ag-Cu	107.4	46.8	1.7	1.6
Ag-Mo	623.8	283.8	0.3	0.0
Ag-Fe	26.5	26.6	24.2	47.8
Ag-Mn	16.7	18.5	19.7	54.0
Ag-Cr	8.1	22.7	34.8	81.1

^a Photocatalyst: 0.5 g; reaction solution: 1 L of aqueous 0.1 M NaHCO₃; CO₂ flow rate: 30 mL min⁻¹; photoirradiation time: 1 h; light source: 400-W high-pressure Hg lamp. Ag-to-M molar ratio: 1.00; Ag@M photodeposition time: 1 h.

and Cr 2p spectra (see Fig. 10(a) and (b), respectively) were obtained, and these reveal that Ag and Cr were present as Ag^0 and Cr^{3+} , respectively, and the intensity ratio of Ag to Cr species was approximately 0.29. After Ar^+ -ion sputtering, peaks corresponding to Cr^0 species were observed in the XPS profile, possibly as a result of the strong reducing power of the Ar^+ -ion sputtering process. However, the Ag-to-Cr ratio (for Cr, both Cr^{3+} and Cr^0) increased to 0.61. Because the escape depth of the electrons excited by X-rays in XPS measurements is generally several nanometers, we believe that the Ag^0 species were covered by a shell of Cr^{3+} species and were exposed after sputtering. After the second cycle of Ar^+ sputtering, the ratio of Ag-to-Cr peak intensities remained at 0.57, indicating that the shell of Cr species on Ag had been almost removed, and the remaining Cr species were located on the surface of the NTO, as depicted in Scheme S1. Furthermore, the modification with Cr^{3+} species improved the photocatalytic stability of the Ag/NTO catalyst, as shown in Fig. 11. Comparing Fig. 7(c–e), it can be seen that the formation of H_2 was suppressed, resulting in stable and high CO selectivity (80.0%). Unlike the Ag/NTO catalyst, for which the Ag nanoparticles were selectively deposited on the (100) facet of NTO on photoirradiation, the Ag@Cr dual cocatalysts showed no preference for any facet (Fig. 12(a)), and the dual Ag@Cr cocatalyst particles were dispersed on both the (100) and (110) surfaces. As discussed Section 3.2, the Ag^0 species loaded on the surfaces of NTO would be redeposited during photoirradiation because of the simultaneous Na^+ leaching and growth of the (110) facets. This probably resulted in the polycrystalline-to-single crystalline transformation of the Ag nanoparticles, as discussed in Section 3.3, which reduced the CO selectivity during the photocatalytic reaction. In contrast, the position, number, and size of the dual Ag-Cr nanoparticles did not change significantly, as shown in Fig. 12(b), suggesting that the Ag nanoparticle morphology was preserved as a result of the Cr^{3+} shell. Therefore, the NTO catalyst modified with Ag and Cr produced CO stably with high selectivity.

4. Conclusion

Ag nanoparticles were loaded on a NaTaO_3 photocatalyst, and their number and size were effectively tuned by varying the photodeposition time and amount of loaded Ag. In addition, surface modification using chromium species was also carried out. We found that the size of the Ag nanoparticles was strongly affected by the photodeposition time, and the largest Ag nanoparticles resulted in the highest CO selectivity in the photocatalytic conversion of CO_2 using H_2O as an electron donor. However, the Ag-loaded NaTaO_3 catalyst showed poor stability in terms of CO selectivity at all Ag loading amounts. We found that the Ag nanoparticles underwent a polycrystalline to single crystalline transition, and the consequent loss of grain boundaries, as well as the changes in the size of the Ag nanoparticles, were responsible for this loss of CO selectivity. The changes to the morphology of the Ag nanoparticles during the photocatalytic reaction could be prevented by covering them with a chromium (III) shell. Using this strategy, the CO selectivity was maintained. By comparison, construction of a Ag@Cr core-shell structure was the best tuning strategy to improve the performances of NaTaO_3 for the photocatalytic conversion of CO_2 by H_2O .

CRediT authorship contribution statement

Xuanwen Xu; Designing and carrying out experiments, Carrying out characterizations, Processing data, Writing original manuscript, Hiroyuki Asakura; Supervision, Reviewing the manuscript, Saburo Hosokawa; Supervision, Reviewing the manuscript, Tsunehiro Tanaka; Supervision, Reviewing the manuscript, Kentaro Teramura; Supervision, Reviewing and Editing the manuscript.

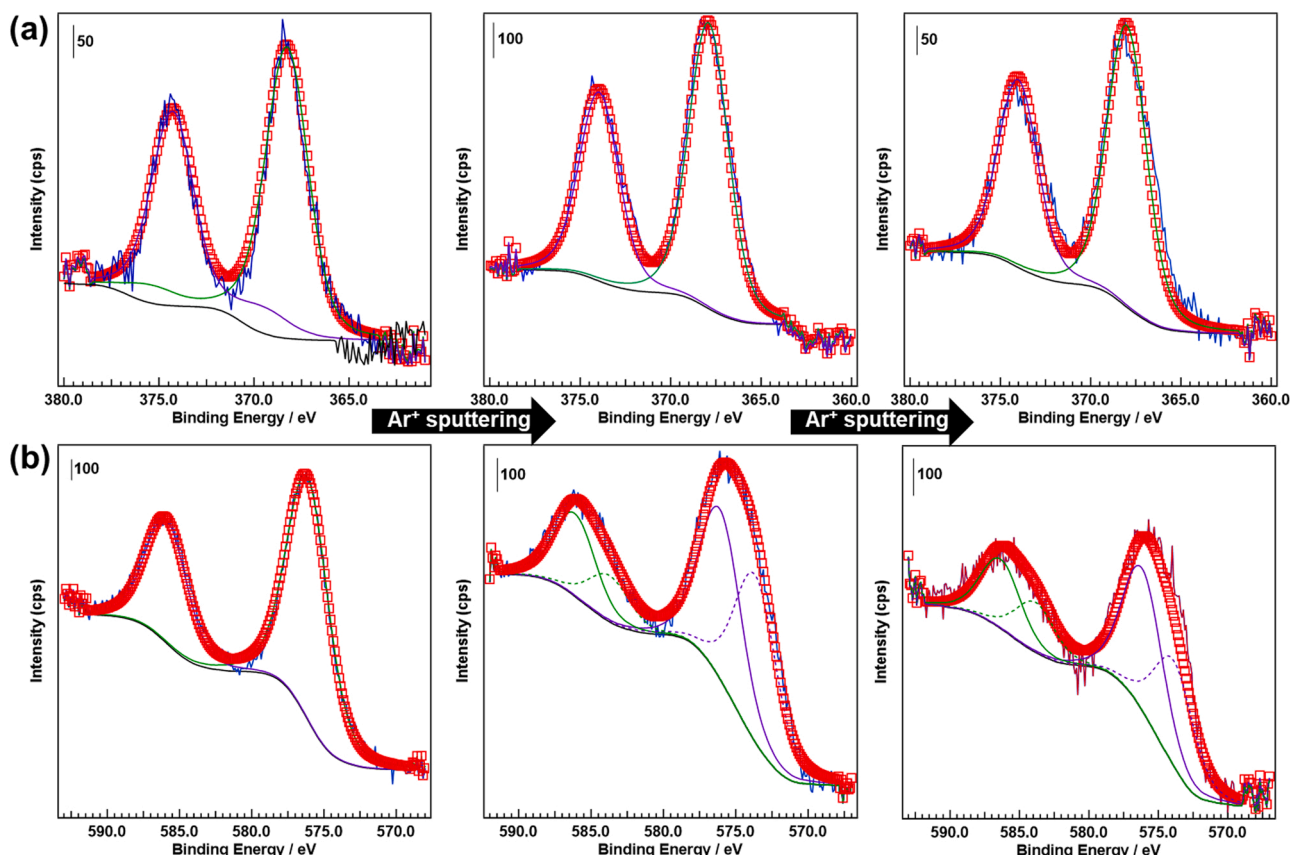


Fig. 10. XPS (a) Ag 3d and (b) Cr 2p spectra of Ag@Cr-loaded NTO.

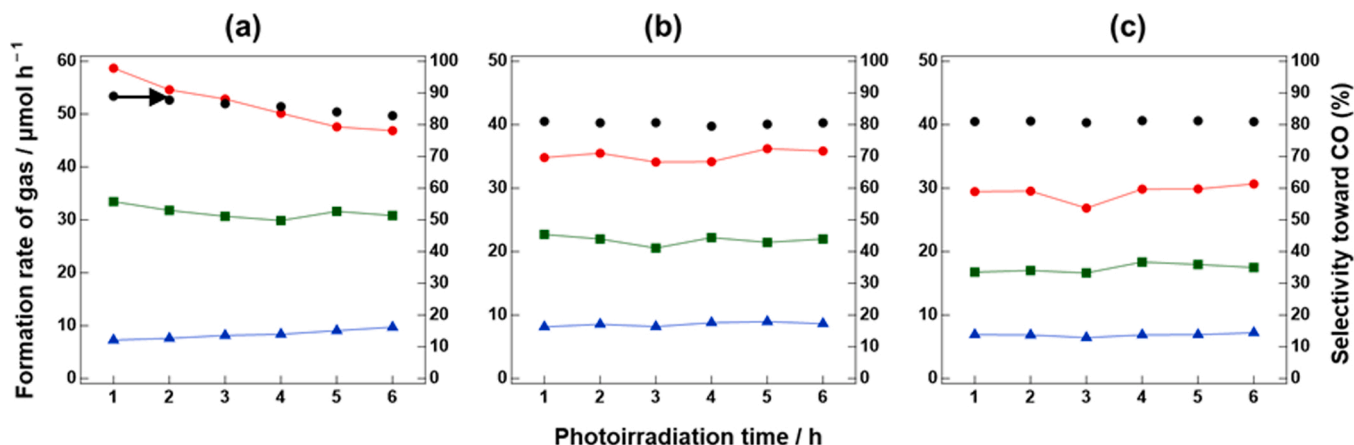


Fig. 11. Formation rates of H₂ (blue), O₂ (green), and CO (red) and CO selectivity (black dots) during the photocatalytic conversion of CO₂ by H₂O over Ag@Cr loaded NTO prepared using different amounts of Ag: (a) 0.1, (b) 0.6, and (c) 1.0 wt%. The molar ratio of AgNO₃ to Na₂CrO₄ was 1.00 in all cases. Reaction conditions: photodeposition time: 1 h; photocatalyst: 0.5 g; reaction solution: 1 L of aqueous 0.1 M NaHCO₃; CO₂ flow rate: 30 mL min⁻¹; light source: 400-W high-pressure Hg lamp.

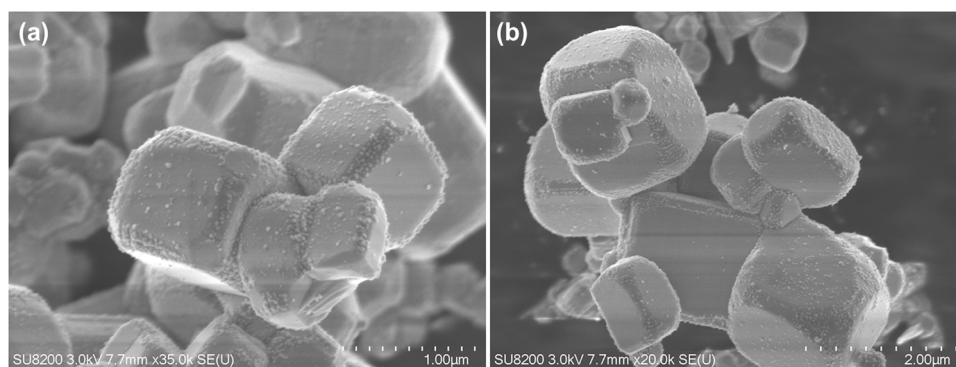


Fig. 12. SEM images of Ag@Cr loaded NTO (a) before and (b) after reaction.

Declaration of Competing Interest

The authors declare that they have no known competing financial interests or personal relationships that could have appeared to influence the work reported in this paper.

Data availability

Data will be made available on request.

Acknowledgement

This study was partially supported by the Program for Elements Strategy Initiative for Catalysts and Batteries (ESICB) commissioned by the Ministry of Education, Culture, Sports, Science, and Technology (MEXT) of Japan. This work was also supported by JSPS KAKENHI Grant Number 21H01716, the Research Grant against Global Warming of the Ichimura Foundation for New Technology, and the CASIO SCIENCE PROMOTION FOUNDATION. Xuanwen Xu thanks the State Scholarship of the China Scholarship Council, which is affiliated with the Ministry of Education of the People's Republic of China.

Appendix A. Supporting information

Supplementary data associated with this article can be found in the online version at [doi:10.1016/j.apcatb.2022.121885](https://doi.org/10.1016/j.apcatb.2022.121885).

References

- [1] A.M. Foley, P.G. Leahy, A. Marvuglia, E.J. McKeogh, *Renew. Energy* 37 (2012) 1–8.
- [2] T.S. Kishore, E.R. Patro, V.S.K.V. Harish, A.T. Haghighi, *Energies* 14 (2021) 2882.
- [3] N. Abbas, A. Kalair, N. Khan, *Futures* 69 (2015) 31–49.
- [4] T.L. Frölicher, M. Winton, J.L. Sarmiento, *Nat. Clim. Change* 4 (2014) 40–44.
- [5] R.W. Miles, G. Zoppi, I. Forbes, *Mater. Today* 10 (2007) 20–27.
- [6] L.I. Granone, F. Sieland, N. Zheng, R. Dillert, D.W. Bahnemann, *Green. Chem.* 20 (2018) 1169–1192.
- [7] T. Hisatomi, J. Kubota, K. Domen, *Chem. Soc. Rev.* 43 (2014) 7520.
- [8] W. Tu, Y. Zhou, Z. Zou, *Adv. Mater.* 26 (2014) 4607–4626.
- [9] A. Li, T. Wang, X.X. Chang, Z.J. Zhao, C.C. Li, Z.Q. Huang, P.P. Yang, G.Y. Zhou, J. L. Gong, *Chem. Sci.* 9 (2018) 5334.
- [10] T. Soltani, A. Yomamoto, S.P. Singh, A. Anzai, E. Fudo, A. Tanaka, H. Kominami, H. Yoshida, *ACS Appl. Energy Mater.* 4 (2021) 6500–6510.
- [11] K. Iizuka, T. Wato, Y. Miseki, K. Saito, A. Kudo, *J. Am. Chem. Soc.* 133 (2011) 20863–20868.
- [12] A. Anzai, N. Fukuo, A. Yamamoto, H. Yoshida, *Catal. Commun.* 100 (2017) 134–138.
- [13] X. Zhu, A. Yamamoto, H. Yoshida, *Dalton Trans.* 50 (2021) 7976–7983.
- [14] X. Zhu, A. Yamamoto, S. Imai, A. Tanaka, H. Kominami, H. Yoshida, *Appl. Catal. B Environ.* 274 (2020), 119085.
- [15] Z. Wang, K. Teramura, S. Hosokawa, T. Tanaka, *J. Mater. Chem. A* 3 (2015) 11313–11319.
- [16] K. Teramura, H. Tatsumi, Z. Wang, S. Hosokawa, T. Tanaka, *Bull. Chem. Soc. Jpn.* 88 (2015) 431–437.
- [17] H. Nakanishi, K. Iizuka, T. Takayama, A. Iwase, A. Kudo, *ChemSusChem* 10 (2017) 112–118.
- [18] S. Iguchi, K. Teramura, S. Hosokawa, T. Tanaka, *Catal. Sci. Technol.* 6 (2016) 4978–4985.
- [19] M. Yamamoto, S. Yagi, T. Yoshida, *Catal. Today* 303 (2018) 334–340.
- [20] X. Zhu, A. Anzai, A. Yamamoto, H. Yoshida, *Appl. Catal. B Environ.* 243 (2019) 47–56.
- [21] S. Wang, K. Teramura, T. Hisatomi, K. Domen, H. Asakura, S. Hosokawa, T. Tanaka, *ACS Appl. Energy Mater.* 3 (2020) 1468–1475.

- [22] S. Wang, K. Teramura, H. Asakura, S. Hosokawa, T. Tanaka, *J. Phys. Chem. C* 125 (2021) 1304–1312.
- [23] Z. Wang, K. Teramura, Z.A. Huang, S. Hosokawa, Y. Sakata, T. Tanaka, *Catal. Sci. Technol.* 6 (2016) 1025–1032.
- [24] R. Pang, K. Teramura, H. Asakura, S. Hosokawa, T. Tanaka, *ACS Sustain. Chem. Eng.* 7 (2019) 2083–2090.
- [25] N. Hoshi, M. Kato, Y. Hori, *J. Electroanal. Chem.* 440 (1997) 283–286.
- [26] M. Ishida, S. Kikkawa, K. Hori, K. Teramura, H. Asakura, S. Hosokawa, T. Tanaka, *ACS Appl. Energy Mater.* 3 (2020) 6552–6560.
- [27] X. Feng, K. Jiang, S. Fan, M.W. Kanan, *J. Am. Chem. Soc.* 137 (2015) 4606–4609.
- [28] R.G. Mariano, K. McKelvey, H.S. White, M.W. Kanan, *Science* 358 (2017) 1187–1192.
- [29] R. Pang, K. Teramura, M. Morishita, H. Asakura, S. Hosokawa, T. Tanaka, *Commun. Chem.* 3 (2020) 1–8.
- [30] S. Wang, K. Teramura, T. Hisatomi, K. Domen, H. Asakura, S. Hosokawa, T. Tanaka, *Chem. Sci.* 12 (2021) 4940–4948.
- [31] X. Zhu, A. Yamamoto, S. Imai, A. Tanaka, H. Kominami, H. Yoshida, *Chem. Commun.* 55 (2019) 13514–13517.
- [32] S. Wang, K. Teramura, T. Hisatomi, K. Domen, H. Asakura, S. Hosokawa, T. Tanaka, *ACS Sustain. Chem. Eng.* 9 (2021) 9327–9335.
- [33] J. Xu, D. Xue, C. Yan, *Mater. Lett.* 59 (2005) 2920–2922.
- [34] W. Chen, Q. Kuang, Z. Xie, *Sci. China Mater.* 58 (2015) 281–288.
- [35] J.H. Yoon, Y. Zhou, M.G. Blaber, G.C. Schatz, S. Yoon, *J. Phys. Chem. Lett.* 4 (2013) 1371–1378.
- [36] M. Sadeghi, W. Liu, T.G. Zhang, P. Stavropoulos, B. Levy, *J. Phys. Chem.* 100 (1996) 19466–19474.
- [37] W.N. Wang, W.J. An, B. Ramalingam, S. Mukherjee, D.M. Niedzwiedzki, *S. J. Am. Chem. Soc.* 134 (2012) 11276–11281.
- [38] W. Yang, W. Ma, Z. Zhang, C. Zhao, *Faraday Discuss.* 210 (2018) 289–299.
- [39] C.W. Li, J. Ciston, M.W. Kanan, *Nature* 508 (2014) 504–507.